



ORIGINAL RESEARCH ARTICLE

Fabrication and Characterization of Ni-, Co-, and Rb-Incorporated $\text{CH}_3\text{NH}_3\text{PbI}_3$ Perovskite Solar Cells

ATSUSHI SUZUKI,^{1,2} MARI OE,¹ and TAKEO OKU¹

1.—Department of Materials Science, The University of Shiga Prefecture, 2500 Hassaka, Hikone, Shiga 522-8533, Japan. 2.—e-mail: suzuki@mat.usp.ac.jp

Ni- and Co-incorporated $\text{CH}_3\text{NH}_3\text{PbI}_3$ perovskite solar cells were fabricated and characterized to optimize the photovoltaic and optical properties related to surface morphology, crystal growth and orientation, and electronic structures. Partially replacing Pb with Ni or Co in the perovskite crystals improved the photovoltaic performance and carrier mobility based on the effective mass in the band structure. In particular, the addition of both Ni and Rb compounds to perovskite improved the long-term stability of the photovoltaic cells, which depended on surface modification and coverage, crystal growth, and the high (100) orientation in the perovskite layer. The short-circuit current density of the cells was increased by promoting the generation and mobility of photoinduced carriers, which were inversely proportional to the effective mass ratio. Electron correlation was associated with the promotion of charge transfer owing to the hybridization between the 3*d* orbitals of Ni and the 5*p* orbitals of the I atoms near the valence band state.

Key words: Perovskite solar cell, nickel, cobalt, rubidium, density functional theory

INTRODUCTION

Inorganic–organic hybrid perovskite solar cells based on mixed-cation and halogen lead hybrid perovskite compounds have been used for practical photovoltaic devices with excellent performance, including high open-circuit voltage (V_{oc}), short-circuit current density (J_{sc}), power conversion efficiency (η), and external quantum efficiency (EQE).^{1,2} The photovoltaic performance and optical properties of perovskite-based solar cells³ depend on perovskite crystal growth, orientation, and elemental composition,^{4–6} type of cell,⁴ morphology, optical absorption coefficient, and carrier mobility, which are related to the excited carrier diffusion length and life in the active and hole-transporting layer (HTL). The general chemical formula of perovskite compounds is ABX_3 , where A and B are cations and X is an anion. In cubic perovskite crystals, the B

cations are surrounded by X anions and the A cations present octahedral coordination. Perovskite crystals consist of Pb atoms at the B-sites, halogen anions (I, Cl, and Br) at the X-sites,^{5,6} and organic cations such as methyl ammonium (MA, CH_3NH_3), formamidinium (FA, $\text{CH}_3(\text{NH}_2)_2$), and guanidinium (GA, $\text{C}(\text{NH}_2)_3$)⁷ at the A-sites. To improve the long-term stability of perovskite-based photovoltaic cells, partial substitution of FA, GA,^{8,9} ionic liquid additives,¹⁰ halogen anions (I^- , Cl^- , and Br^-),¹¹ alkali metal ions (Na^+ , K^+ , Rb^+ , and Cs^+),^{12–16} metals (Sn and Pb),¹⁷ transition metals (Cu,^{18–22} Co,^{23,24} Ni,²⁵ Zn,^{26,27} Cr,²⁸ Y, Fe, and Mn²⁹ in perovskite crystals has been investigated. The tolerance factor varied with the effective ionic radii of transition metals and was used to predict the thermodynamic stability of single perovskite cubic crystals.³⁰

Transition metal-incorporated perovskite crystals promote photoinduced carrier generation and diffusion and increase the optical absorption coefficient and wavelength related to the E_g of perovskites.^{18–29} Uniform crystalline films without defects and pinholes effectively promote carrier generation and

diffusion without carrier recombination, which improves the long-term stability of perovskite-based photovoltaic cells under atmospheric conditions. For example, the addition of small amounts of Co^{23,24} or Ni²⁵ to perovskite crystals improved crystal nucleation and growth by increasing surface coverage, which caused an increase in photocurrent by suppressing the leakage current near the interface between the crystal domains. The immobilization of defects by suppressing carrier traps was performed to improve photovoltaic performance.^{24,25} Based on electronic structural analysis, carrier mobility related to the effective mass was expected by the band dispersion of the perovskite crystals along the direction of the wave vector. Additionally, perturbation of crystal field splitting via the Jahn–Teller effect is an important factor for controlling the splitting of the degenerate energy levels of the 3*d* orbitals and charge transfer between the 3*d* orbitals of transition metals and the 5*p* orbitals of halogen atoms in the coordination structure.^{18–21,26–31} Recently, the addition of small amounts of Eu³⁺–Eu²⁺ ions to perovskite crystals improved the long-term stability of perovskite-based photovoltaic cells by decreasing the number of internal defects and suppressing degradation via redox shuttle reactions.³² Experimental results and theoretical first-principle density functional theory (DFT) calculations revealed that the electronic structure of lanthanide- and actinide-containing perovskite compounds could be optimized by tuning their photovoltaic and optical properties.^{31,32} Eu and acetate codoped perovskite solar cells with high conversion efficiency and stability have been fabricated and characterized.³³

Furthermore, the incorporation of small amounts of alkali metals, such as K, Na, Rb, and Cs, in uniform crystalline perovskite films, crystal growth, and suppression of pinholes and defects improved the photovoltaic performance of perovskite-based solar cells. Photoinduced current density–voltage (*J*–*V*) curve analysis, infrared (IR) and Raman spectroscopy,^{34–36} nuclear magnetic resonance (NMR) spectroscopy,^{37–40} scanning probe microscopy with energy-dispersive x-ray spectroscopy,⁴¹ x-ray diffraction (XRD) analysis, crystal structure analysis, and angle-resolved photoemission spectroscopy⁴² have been used to optimize the photovoltaic and optical properties of perovskite-based solar cells. The electronic structure, band gap (E_g), effective mass of electrons (m_e^*) and holes (m_h^*), total density of states and partial density of states (PDOS) have been analyzed using first-principles DFT calculations.^{43–46} Electron correlation was associated with the charge transfer from the alkali metal to the Pb atom near the conduction band (CB) and ligand-to-metal charge transfer from the I atom to the metal near the valence band (VB). The electronic mechanism was based on the promotion of carrier generation, diffusion in the perovskite layer, and crystal growth and orientation, which were expected to improve the photovoltaic

performance of the cell in terms of short-circuit current density and conversion efficiency. The Gibbs free energy (ΔG) and entropy (ΔS) values suggested that thermodynamic stabilization occurred without carrier diffusion scattering as phonon effectiveness.^{30,43,44} The ΔS value and vibration modes in the IR and Raman spectra were considered with the electron–lattice interaction as the phonon effect.

The goal of this study was to investigate the effects of the addition of transition metals on the photovoltaic and optical properties, microstructure, and electronic structure of methylammonium lead iodide (MAPbI_3) perovskite-based solar cells. The effects of adding Co, Ni, and Rb to MAPbI_3 perovskite compounds on the long-term stability of the photovoltaic cells and on perovskite microstructure, crystal growth, and electronic structure were investigated experimentally and using first-principles DFT calculations. The photovoltaic mechanism was discussed based on the band structure using m_e^* , m_h^* , E_g , the PDOS, and electron correlation associated with the 3*d* hybrid orbitals of the transition metal and 5*p* orbitals of the I atom near the VB.

EXPERIMENTAL

The schematic diagram for the fabrication of Co-, Ni-, and Rb-incorporated MAPbI_3 perovskite solar cells is presented in Fig. 1. Fluorine-doped tin oxide (FTO) substrates (FNT1.6, 20 mm × 20 mm × 1.6 mm, Nippon Sheet Glass Company, Ltd.) were cleaned in an ultrasonic bath using acetone and methanol and were subsequently dried under a N_2 flow. TiO_x precursor solutions (0.15 and 0.30 M) were prepared using titanium diisopropoxide bis(acetylacetonate) (0.055 and 0.11 mL, respectively, Sigma-Aldrich) and 1-butanol (1 mL, Nacalai Tesque). Thereafter, the 0.15 M TiO_x precursor solution was spin-coated on the FTO substrate at 3000 rpm for 30 s followed by annealing at 125°C for 5 min. Subsequently, the 0.30 M TiO_x precursor solution was spin-coated on the previously deposited TiO_x layer at 3000 rpm for 30 s followed by annealing at 125°C for 5 min. This process was performed twice, and then, the fabricated FTO substrate was sintered at 500°C for 30 min to form a compact TiO_2 layer. To obtain a mesoporous TiO_2 layer, TiO_2 paste was prepared by mixing TiO_2 powder (Aeroxide TiO_2 P-25, Evonik Industries AG) with polyethylene glycol (PEG #20000, Nacalai Tesque) in ultrapure water. The solution was mixed with acetyl acetone (Wako Pure Chemical Industries) and Triton X-100 (Sigma-Aldrich) for 30 min and was allowed to rest for 12 h to suppress the formation of bubbles. To prepare the electron-transporting layer, TiO_2 paste was coated on the substrate by spin-coating at 2000 rpm for 5 s and then at 5000 rpm for 30 s. The prepared cells were annealed at 120°C for 5 min and at 550°C for 30 min to form mesoporous TiO_2 layers.

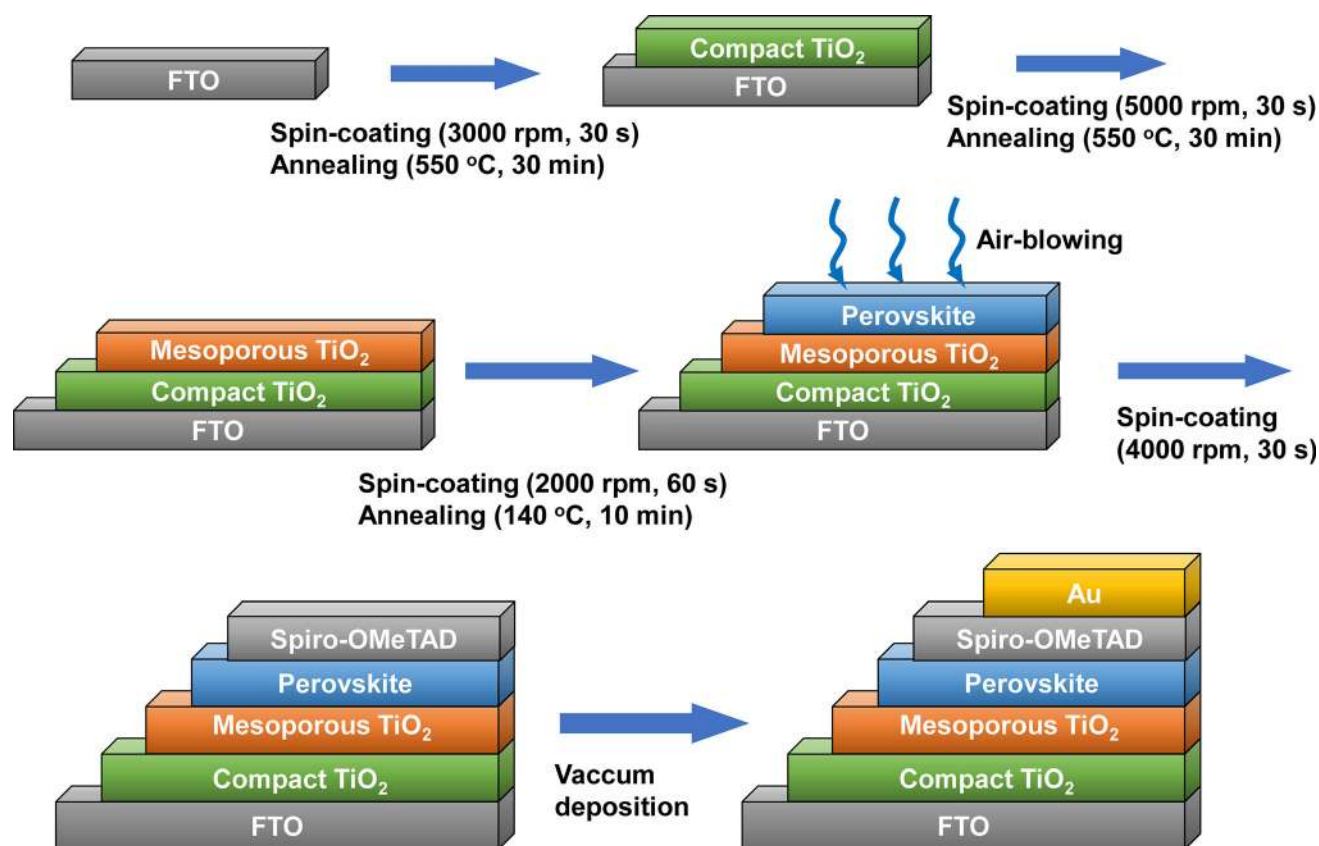


Fig. 1. Fabrication of Co-, Ni-, and Rb-incorporated MAPbI₃ perovskite solar cells.

To synthesize the perovskite compounds, a solution of methylamine hydroiodide (MAI: 190.7 mg, 1.2 mmol, Tokyo Chemical Industry Co., Ltd.) and lead(II) chloride (PbCl₂, 111.2 mg, 0.4 mmol, Sigma-Aldrich) in *N,N*-dimethylformamide (500 μ L, Nacalai Tesque) was mixed with 1, 2, or 5 wt.% cobalt(II) chloride (CoCl₂, Sigma-Aldrich) or nickel(II) chloride anhydrous (NiCl₂, Tokyo Chemical Industry Co., Ltd.) and rubidium iodide (RbI, Wako Pure Chemical Industries) at 60 °C for 24 h. Subsequently, the perovskite solution was added to the TiO₂ mesoporous film via spin-coating. The spin-coating speed was maintained at 1000 rpm for 5 s and then at 2000 rpm for 60 s; moreover, a heat gun placed 25 cm away from the surface of the film was used to generate a 60 s hot air burst. After spin-coating, the samples were subjected to annealing at 140 °C for 10 min. The HTL was prepared and spin-coated as follows. A solution of 2,2',7,7'-tetrakis[*N,N*-di(methoxyphenyl)amino]-9,9'-spirobifluorene (Spiro-OMeTAD, 36.1 mg, Wako Pure Chemical Industries) in chlorobenzene (0.5 mL, Wako Pure Chemical Industries) was mixed with a solution of lithium bis(trifluoromethyl sulfonyl)imide (Li-TFSI, 260 mg, Tokyo Chemical Industry Co., Ltd.) in acetonitrile (0.5 mL, Nacalai Tesque) for 12 h. The solution obtained by adding 4-tert-butylpyridine (14.4 μ L, Sigma-Aldrich) to the Spiro-OMeTAD solution was mixed with the Li-

TFSI solution (8.8 μ L) for 30 min at 70 °C. The obtained mixture was spin-coated at 2000 rpm for 5 s and then at 4000 rpm for 30 s. All experiments were performed under atmospheric conditions. Lastly, a layer of Au was deposited via evaporation on the top side of the electrodes. The layered structure of the photovoltaic cells was denoted as FTO/TiO₂/perovskite/Spiro-OMeTAD/Au (Fig. 1).

The *J*-*V* curves of the photovoltaic cells were obtained under an illumination of 100 mW cm⁻² using an AM 1.5 solar simulator (San-ei Electric XES-301S) at 27 °C. The solar cells were illuminated through the side of the FTO substrates, and the illuminated area was 0.090 cm². The average power conversion efficiency (η_{ave}) was estimated using the average of the forward and reverse values. The reverse value was used as the best efficiency. Several *J*-*V* curves were obtained to determine the average and highest values. The long-term stability of the cells and changes in η and J_{sc} were analyzed at 27 °C and 20% humidity for 50 d. The η_{ave} values were estimated using a three-electrode system. The yield value was removed when the surface was damaged. The incident photon-to-current efficiencies of the cells were also investigated using a QE-R (Enli Technology) system. The microstructure of the perovskite thin films was observed using an Eclipse E600 (Nikon) optical microscope. The crystal structure, crystallinity, and

lattice spacing of the perovskite thin films were measured using a D2 Phaser (Bruker) XRD system. After removing the $\text{K}\alpha_2$ x-ray wavelength of the Cu target from the measured x-ray diffraction patterns, the crystallite sizes were estimated using the Scherrer formula, the Scherrer constant ($K = 0.9$), and device constant ($\beta = 0.065$). The crystal structure of each perovskite crystal was confirmed using data reported in the literature.³⁰

The electronic structures of the perovskite crystals were single-point-calculated using the crystallographic structural data obtained from their XRD patterns. Ab initio quantum calculations were performed using the Vanderbilt ultrasoft pseudo-potentials, scalar relativistic generalized gradient approximations and Perdew–Burke–Ernzerhof (GGA-PBE) exchange-correlation functional (Quantum Espresso software) without considering the spin–orbital coupling effect. The plane-wave basis set cutoffs for the wave functions and charge density were set at 25 and 225 Ry. A uniform k -point grid ($4 \times 4 \times 4$) in the Brillouin zone was used to calculate the electronic structure and PDOS. The perovskite crystals presented cubic symmetry with $Pm\bar{3}m$ space group, and $2 \times 2 \times 2$ cubic supercells were constructed using the experimental lattice constant determined utilizing XRD data. In the metal-incorporated perovskite crystal unit cell model, a fraction of the Pb atoms at the B-sites was substituted with Co or Ni atoms for one-atom substitution at the center of the cubic structure. Co- or Ni-incorporated MAPbI_3 perovskite cubic crystal models were constructed using $2 \times 2 \times 2$ supercells and the experimentally determined lattice constants, and the models were used for band calculations. The molar ratio of Co^{2+} or Ni^{2+} ions to Pb^{2+} ions was adjusted to 1:8; that is, 12.5% of Pb^{2+} ions were replaced with Co^{2+} or Ni^{2+} ions. The ion replacement and structural distortion caused by the difference in the ionic radii of Co^{2+} or Ni^{2+} and Pb^{2+} worked slightly in the isolated dilution system. The band structures, effective mass, and band gap of the Brillouin zone of the perovskite crystal lattice were analyzed along the direction of the wave vector. The path for MAPbI_3 perovskite crystal was set as follows: Γ (0, 0, 0) \rightarrow X (0, $\frac{1}{2}$, 0) \rightarrow M ($\frac{1}{2}$, $\frac{1}{2}$, 0) \rightarrow Γ \rightarrow R ($\frac{1}{2}$, $\frac{1}{2}$, $\frac{1}{2}$) \rightarrow X, M \rightarrow R, and the path for the $\text{MAPb}(\text{Co})\text{I}_3$ and $\text{MAPb}(\text{Ni})\text{I}_3$ perovskite crystals were set as follows: Γ (0, 0, 0) \rightarrow X ($\frac{1}{2}$, 0, $\frac{1}{2}$) \rightarrow W ($\frac{1}{2}$, $\frac{1}{4}$, $\frac{3}{4}$) \rightarrow K ($\frac{3}{8}$, $\frac{3}{8}$, $\frac{3}{4}$) \rightarrow Γ \rightarrow L ($\frac{1}{2}$, $\frac{1}{2}$, $\frac{1}{2}$) \rightarrow U ($\frac{5}{8}$, $\frac{1}{4}$, $\frac{5}{8}$) \rightarrow W ($\frac{1}{2}$, $\frac{1}{4}$, $\frac{3}{4}$) \rightarrow L \rightarrow K|U \rightarrow X. The effective m_e^*/m_0 and m_h^*/m_0 ratios, where m_0 is the mass of free electrons, were calculated using the curvature of the band dispersion curve. The Fermi energy was set to zero. The density of states (DOS) and PDOS were calculated to determine the energy level of each orbital near the VB and CB. The experimentally determined band structure of the cubic crystals was compared

with the theoretical and experimental results reported in the literature.

To assess the thermodynamic stability and electron–lattice interactions as the phonon effect in the systems with added Co or Ni, the thermodynamic parameters and vibration modes in the IR and Raman spectra were analyzed using hybrid DFT utilizing the unrestricted B3LYP (UB3LYP) with LANL2MB basis set (Gaussian 09). The cluster model of the perovskite crystals consisted of a cubic crystal, and its lattice constants were experimentally determined using XRD data. The metal-incorporated MAPbI_3 cubic structure and MAPbI_3 perovskite crystal cluster models were constructed using $2 \times 2 \times 2$ supercells, which were fixed at +8 as the positive charge of MA. The thermodynamic parameters (ΔG , enthalpy (ΔH), and ΔS) and the vibration modes in the IR and Raman spectra of the cluster model metal-incorporated MAPbI_3 perovskite cubic crystals with $2 \times 2 \times 2$ supercells were calculated using hybrid DFT utilizing the frequency mode. The effects of incorporating Co or Ni atoms into the perovskite crystals on the photovoltaic properties of the perovskite-based cells were qualitatively investigated using experimental data, electronic structure, and thermodynamic properties.

RESULTS AND DISCUSSION

The photovoltaic properties of perovskite-based solar cells were investigated using the J – V curves obtained under illumination. The J – V curves of the solar cells featuring Co-, Ni-, Co/Rb-, and Ni/Rb-incorporated MAPbI_3 perovskites are presented in Fig. 2. The J_{sc} and V_{oc} values indicated that the cells presented semiconductive characteristics. The photovoltaic parameters, namely V_{oc} , J_{sc} , fill factor (FF), series resistance (R_s), shunt resistance (R_{sh}), and η , of all analyzed cells are listed in Table I. The

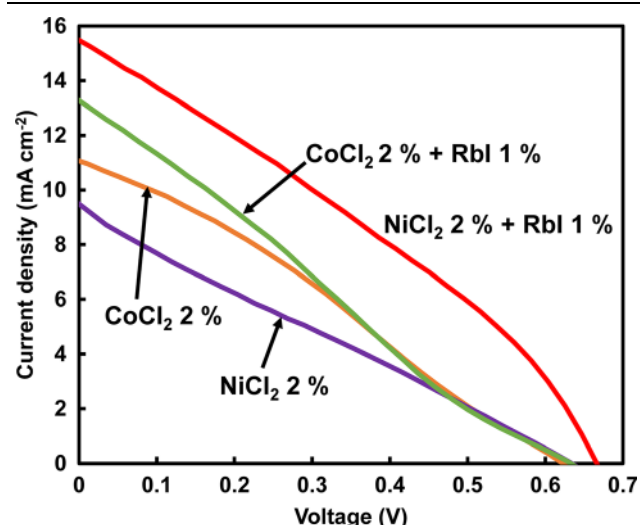


Fig. 2. J – V characteristics of the perovskite solar cells with CoCl_2 , NiCl_2 and RbI.

Table I. Photovoltaic parameters of Co-, Ni- and Rb-incorporated MAPbI₃ perovskite solar cells

Devices	J_{sc} (mA cm ⁻²)	V_{oc} (V)	FF	R_s (Ω cm ²)	R_{sh} (Ω cm ²)	η (%)	η_{ave} (%)
MAPbI ₃	18.2	0.807	0.503	7.43	175	7.40	6.75
CoCl ₂ 2%	11.1	0.623	0.287	40.8	91.6	1.98	1.73
NiCl ₂ 2%	9.49	0.634	0.248	47.8	76.4	1.49	1.31
CoCl ₂ 5%	15.1	0.800	0.381	24.2	340	4.60	3.53
NiCl ₂ 5%	17.2	0.514	0.343	16.7	110	3.04	2.38
CoCl ₂ 2% + RbI 1%	13.3	0.633	0.246	38.3	53.8	2.07	1.77
NiCl ₂ 2% + RbI 1%	12.5	0.679	0.401	13.1	117	3.40	3.19
CoCl ₂ 5% + RbI 2%	11.1	0.831	0.392	13.1	154	3.58	3.30

addition of 2 or 5% NiCl₂ or CoCl₂ to MAPbI₃ perovskite affected the photovoltaic parameters and caused the J_{sc} , V_{oc} , FF, and η values of the cells featuring Ni- or Co-incorporated MAPbI₃ perovskites to be lower than those of the cells featuring MAPbI₃ perovskite crystals. When 2% CoCl₂ or NiCl₂ and 1% RbI were co-added to MAPbI₃ perovskite, the η value of the cells increased to 2.07–3.58 %. J_{sc} , V_{oc} , and R_{sh} increased with the amount of CoCl₂ when different amounts of CoCl₂ and 1% RbI were co-added to MAPbI₃ perovskite. The photovoltaic performance of cells was improved via surface modification and crystal growth promotion in the perovskite layer. The J_{sc} , V_{oc} , FF, and η values were lower than those of the cells featuring tetragonal MAPb_{0.984}Co_{0.016}I₃^{23,24} and Ni-doped MAPbI₃²⁵ perovskite crystals. The replacement of Pb with Co or Ni affected the surface morphology and the growth of perovskite crystals and also the cubic-to-tetragonal phase transition. The photovoltaic performance of the cells featuring perovskites with added Co or Ni depended on promoting crystal growth and hindering the formation of pinholes and defects.

The EQEs of the solar cells featuring Co/Rb- and Ni/Rb-incorporated MAPbI₃ perovskite perovskites are illustrated in Fig. 3a and b. The performance of these cells was compared with that of the cell featuring MAPbI₃ perovskite and Co- and Ni-incorporated MAPbI₃ perovskites. The addition of CoCl₂ or NiCl₂ to MAPbI₃ perovskite decreased the EQE to 400–800 nm. The EQEs of these cells were lower than those of the cells featuring MAPb(Co)I₃²³ and MAPb(Ni)I₃ perovskite layers.²⁵ In this study, the photons did not efficiently convert into current, and J_{sc} and η decreased. Carrier recombination and loss occurred near the interfaces with defects and pinholes in the cubic-phase perovskite layer. E_g was estimated using the alignment of band edges in EQE. The E_g values of MAPb(Co)I₃ and MAPb(Ni)I₃ were determined to be 1.547 and 1.545 eV, respectively, which were lower than that of the MAPbI₃ crystal (1.563 eV, Table IV). The E_g values of MAPb(Co)I₃ and MAPb(Ni)I₃ were slightly underestimated compared with those of the recently reported cells featuring MAPb(Co)I₃ or MAPb(Ni)I₃ crystals (1.56 eV²³ and 1.58 eV,²⁵ respectively). The

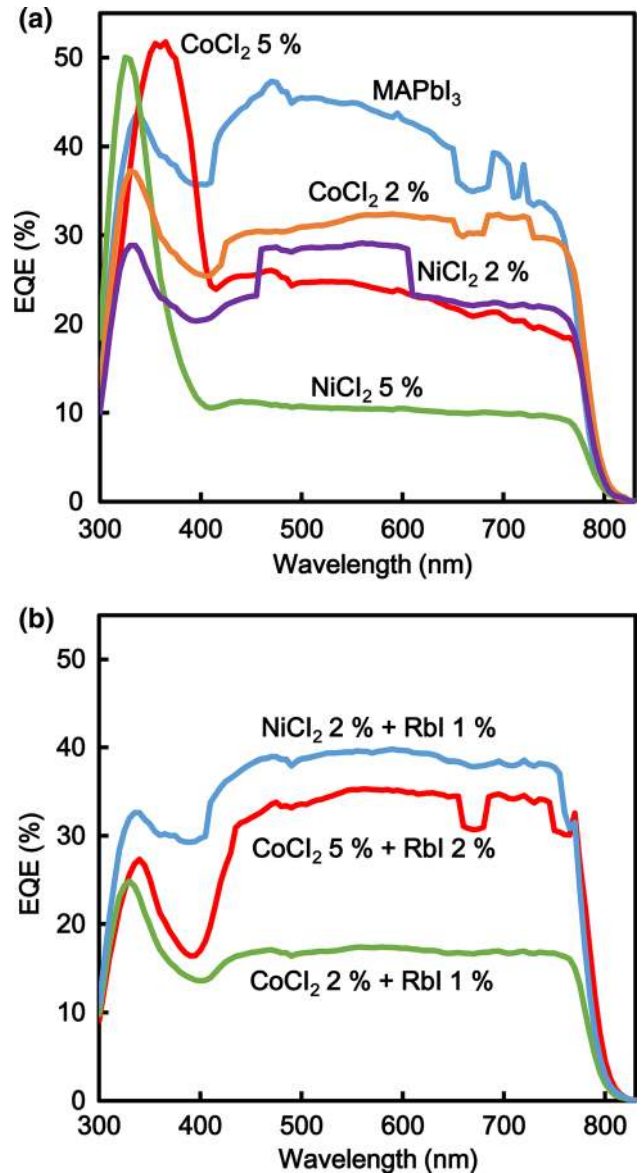


Fig. 3. External quantum efficiency of the perovskite solar cells with (a) CoCl₂, NiCl₂, and (b) RbI.

experimental behavior of the cells was discussed based on the band structure, effective mass, and E_g . The addition of Co or Ni to the MAPbI₃ perovskite

crystals affected the internal structure, crystal growth, electron structure, and E_g , which was related to the energy levels of the VB.²³ The band structure near the VB was attributed to the effect of the Jahn–Teller distortion on energy level splitting, and the hybridization of the $3d$ orbitals of the transition metal with the $5p$ orbitals of the I^- ions, which served as ligands in the coordination structure.

The changes in η and J_{sc} of perovskite solar cells were analyzed at 27°C and 20% humidity for 50 d, as illustrated in Fig. 4a and b. The co-addition of 2% NiCl_2 and 1% RbI increased η and J_{sc} after 36 d. When 2% NiCl_2 and 1% RbI were co-added to MAPbI_3 perovskite, η and J_{sc} increased significantly

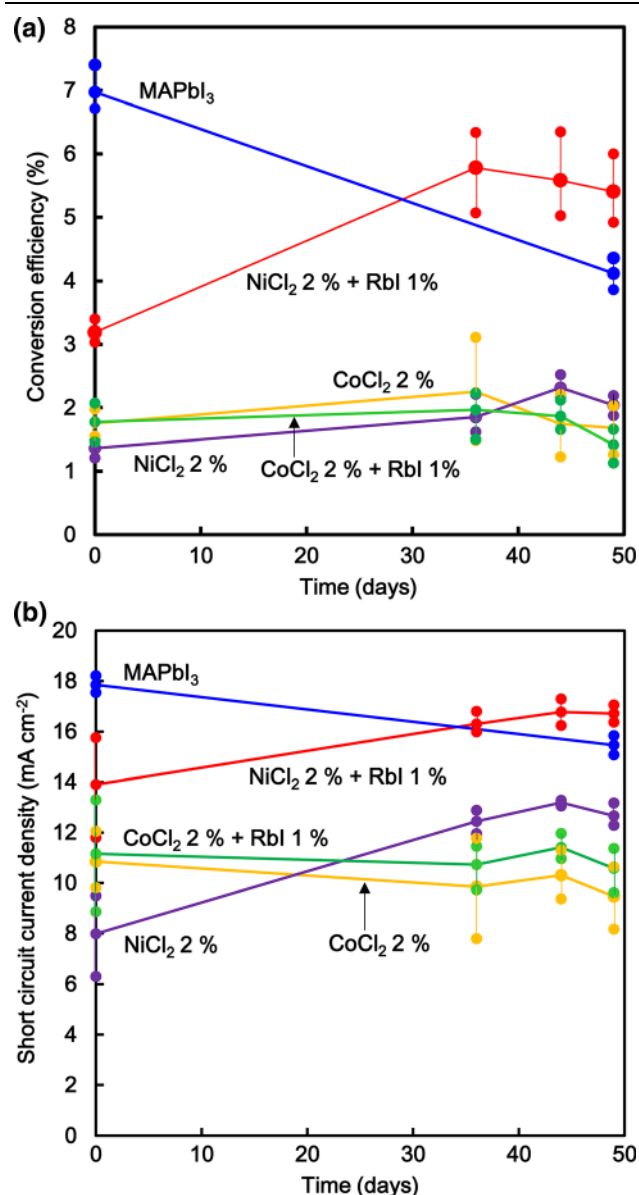


Fig. 4. Long-term stability of (a) conversion efficiencies and (b) short-circuit current densities for the perovskite solar cells. The solar cells were stored and characterized at temperature of 27°C and humidity of 20%. The average values of η and J_{sc} were estimated from the three electrodes in the devices.

from 3.19% to 5.78% and from 13.91 mA cm^{-2} to 16.30 mA cm^{-2} , respectively, in 36 d. The increase in J_{sc} and η was attributed to carrier diffusion promotion in the perovskite crystal with the co-addition of NiCl_2 and RbI owing to the solid-phase reaction with diffusion in the perovskite layer compared with the slow deterioration behavior of MAPb(Ni)I_3 for 150 h.²⁵ For the MAPbI_3 solar cells, η and J_{sc} suddenly decreased from 6.97% to 4.12% and from 17.85 mA cm^{-2} to 15.5 mA cm^{-2} , respectively, after 49 days (Fig. 4b and c). This reduced performance was ascribed to the decrease in photocurrent with carrier recombination near defects and the interface while causing a decomposition reaction with diffusion of MA cations and halogen anions for the long-term period.

The XRD patterns, crystal sizes, and lattice constants of the solar cells featuring CoCl_2 -, NiCl_2 -, CoCl_2/RbI -, and NiCl_2/RbI -incorporated MAPbI_3 perovskites are presented in Fig. 5a and b and Table II. The XRD patterns of the MAPbI_3 perovskite crystals were in good agreement with data reported in the literature.³⁰ The strong diffraction peak at 2θ corresponded to the d -spacing of 6.271 Å, which was assigned to the (100) plane of the cubic perovskite crystals. The intensity of the peak at 2θ increased with increasing amounts of CoCl_2 and NiCl_2 (Fig. 5a and b). Table II summarizes the crystallite sizes, lattice constants, crystal systems, and unit cell volume per number of formula units in the cells of CoCl_2 -, NiCl_2 -, CoCl_2/RbI -, and NiCl_2/RbI -incorporated MAPbI_3 perovskite crystals. The crystallite sizes of the MAPbI_3 perovskites incorporated with 5% CoCl_2 or 5% NiCl_2 (954 and 1079 Å, respectively) were larger than that of pristine MAPbI_3 perovskite (644 Å). The lattice constants of the (100) plane of the MAPbI_3 perovskites incorporated with 5% CoCl_2 or 5% NiCl_2 (6.285 Å and 6.273 Å, respectively) were larger than that of pristine MAPbI_3 perovskite (6.271 Å). Similarly, the co-addition of 2% CoCl_2 and 1% RbI or 2% NiCl_2 and 1% RbI to MAPbI_3 perovskite increased the crystallite size and lattice constant of the (100) plane.

The changes in crystal structure, growth, and phases of the perovskite crystals with the addition of Co or Ni in this study were different from those reported in the literature (Table II).^{23–25} When 1.6 and 3.1% Co^{2+} ions were added to MAPbI_3 perovskite, the as-grown MAPbCoI_3 crystals presented a tetragonal phase.^{23,24} When 3% NiCl_2 was added to MAPbI_3 perovskite, the as-grown MAPbNiI_3 crystals presented a tetragonal phase and high crystallinity.²⁵ Annealing confers thermodynamic stability, surface morphology, crystal structure, crystallinity, and phase. In this study, annealing at 140°C led to transition into a stable cubic crystal phase. Annealing at temperatures above the phase transition temperature affected crystal growth and the phase related to J_{sc} and η .

The unit cell volume per number of formula units slightly increased with increasing the percentages

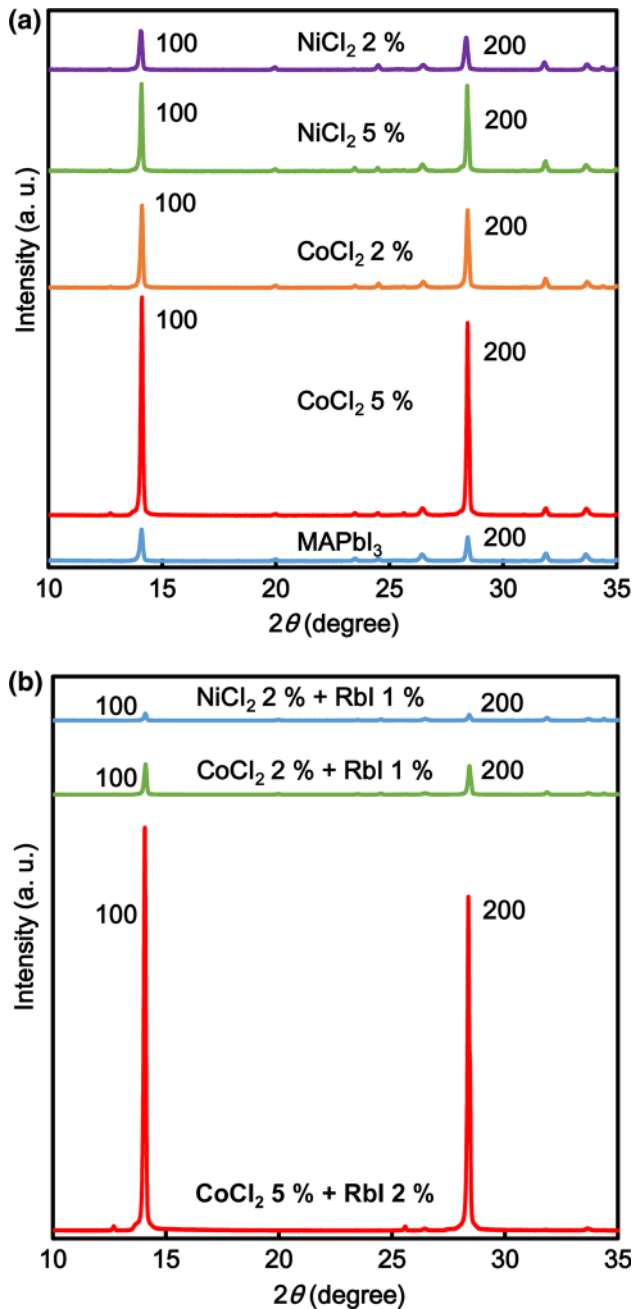


Fig. 5. X-ray diffraction patterns of the perovskite solar cells with (a) CoCl₂, NiCl₂, and (b) RbI.

of CoCl₂, NiCl₂, and RbI, even though the ionic radii of Co²⁺ and Ni²⁺ ions (0.75 and 0.69 Å, respectively) are smaller than that of Pb²⁺ ions (1.19 Å), and the radius of Rb⁺ ions (1.72 Å) is smaller than that of MA⁺ ions (2.17 Å). The perovskite layer contained numerous defects and voids. The incorporation of small amounts of Co or Ni improved crystal nucleation and growth by suppressing the formation of vacancy defects near grain boundaries and short-range order of the crystal structure in the perovskite layer; this enhanced the stability and the strength of the chemical bonds between the Ni²⁺ or Co²⁺ ions and I⁻ ions in octahedral coordination.^{24,47}

The co-addition of small amounts of CoCl₂ and RbI or NiCl₂ and RbI markedly improved crystal orientation and growth and suppressed grain boundaries in the perovskite layer. Rb occupied the MA defects within the perovskite crystals and promoted crystal nucleation and growth in the perovskite layer.¹⁶ The crystal growth in the perovskite layer reduced the trap density between perovskite grains and increased J_{sc} and η . The Ni/Rb-incorporated MAPbI₃ perovskite crystal presented a stable η .

The optical microscopy images of the solar cells featuring MAPbI₃ perovskite, CoCl₂-incorporated MAPbI₃ perovskites, NiCl₂-incorporated MAPbI₃ perovskites, CoCl₂/RbI-incorporated MAPbI₃ perovskites, and NiCl₂/RbI-incorporated MAPbI₃ perovskites are presented in Fig. 6. Uniform and dense crystal films with high surface coverage were obtained when 5% CoCl₂ and 2% RbI were co-added to MAPbI₃ perovskite. For the MAPb_{0.9}Co_{0.1}I₃ thin film, the number of voids and defects was low, which promoted crystal nucleation and growth. Surface modification with crystal growth improved the photovoltaic performance of the cells. Surface morphological observation and XRD analysis were performed after long-term cell use. The crystallinity, surface morphology, particle size, and surface coverage of the perovskite-based solar cells after long-term use are presented in Fig. 7a and b. The intensity of the peak ascribed to the (100) crystal plane of the MAPbI₃ perovskite crystal co-added with 2% NiCl₂ and 1% RbI increased after 44 days of use; moreover, the I_{100}/I_{210} ratio increased from 2.59 to 3.35. In comparison, the I_{100}/I_{210} ratio of the solar cell featuring MAPbI₃ perovskite increased from 4.10 to 4.93. Typically, a I_{100}/I_{210} ratio of 2.1 corresponds to random crystal orientation. These results indicated that crystals with (100) orientation grew on the perovskite layer after 44 days of use. The co-addition of 2% NiCl₂ and 1% RbI to MAPbI₃ perovskite promoted particle growth and passivation and suppressed decomposition. The particle size and surface coverage of the MAPbI₃ perovskite incorporated with 2% NiCl₂ and 1% RbI increased from 14.5 μm to 25.1 μm and from 70.3 μm to 84.7 μm, respectively, after 60 days of use. Conversely, for the solar cell featuring pristine MAPbI₃ perovskite, the particle size and surface coverage decreased from 13.0 μm to 3.4 μm and from 61.5 μm to 48.2 μm, respectively. These results indicated the suppression of crystal nucleation and growth with decreasing particle size. The changes in crystalline surface morphology and crystal growth after long-term aging are illustrated in Fig. 8. The co-addition of NiCl₂ and RbI to MAPbI₃ perovskite improved the growth of crystals with (100) orientation. The promotion of crystal growth and orientation without defects and pinholes improved the long-term stability of the photovoltaic cells and suppressed the decomposition reaction and ion diffusion (Table III).

Table II. Crystallite sizes and lattice constants of the perovskite crystals

Perovskite	Crystallite size (Å)	Lattice constant (Å)	Ref.	Crystal system (space group)	Unit cell volume (Å ³)/Z***
MAPbI ₃	644	6.271(2) 6.2842(1)*	Present work 23	Cubic (<i>Pm</i> $\bar{3}$ <i>m</i>)	246.63 248.72*
Additives					
CoI ₂ 1.6%*		<i>a</i> = 8.88457(1)* <i>c</i> = 12.6034(5)	23	Tetragonal (<i>I4/mcm</i>)	248.72*
CoCl ₂ 2%	814	6.272	Present work 23	Cubic (<i>Pm</i> $\bar{3}$ <i>m</i>)	246.73
CoI ₂ 3.1%*		<i>a</i> = 8.88624(5)* <i>c</i> = 12.6134(0)		Tetragonal (<i>I4/mcm</i>)	249.01*
CoCl ₂ 5%	955	6.285	Present work	Cubic (<i>Pm</i> $\bar{3}$ <i>m</i>)	248.27
NiCl ₂ 2%	608	6.285(1)	Present work 25	Cubic (<i>Pm</i> $\bar{3}$ <i>m</i>)	248.28
NiCl ₂ 3%**		<i>a</i> = 8.8758** <i>c</i> = 12.6283		Tetragonal (<i>I4/m</i>)	248.72**
NiCl ₂ 5%	1079	6.273(1)	Present work	Cubic (<i>Pm</i> $\bar{3}$ <i>m</i>)	246.86
CoCl ₂ 2% + RbI 1%	729	6.274	Present work	Cubic (<i>Pm</i> $\bar{3}$ <i>m</i>)	246.96
NiCl ₂ 2% + RbI 1%	771	6.275	Present work	Cubic (<i>Pm</i> $\bar{3}$ <i>m</i>)	247.08
CoCl ₂ 5% + RbI 2%	1239	6.284(2)	Present work	Cubic (<i>Pm</i> $\bar{3}$ <i>m</i>)	248.17

*Ref. 23, **Ref. 25.

***Z is the number of formula units in a unit cell.

The band structures near the VB and CB of the MAPbI₃, MAPb(Co)I₃, and MAPb(Ni)I₃ perovskite crystals are presented in Fig. 9. The band dispersions and band gaps of the Brillouin zone of the perovskite crystal lattice along the direction of the wave vector were analyzed. The band along of the Γ (0, 0, 0) direction in the MAPb(Ni)I₃ perovskite crystal presented a strong dispersion similar to that of the *R* (1/2, 1/2, 1/2) direction in the MAPbI₃ perovskite crystal (Fig. 9). The band of the MAPb(Co)I₃ perovskite crystal was widely dispersed along the direction. The partial replacement of Pb in the perovskite crystal with Co or Ni affected the energy dispersion near the VB and CB by narrowing the band gap. The m_e^*/m_0 and m_h^*/m_0 values are listed in Table IV. The m_e^*/m_0 values of all analyzed systems presented the same order of magnitude. The calculated values revealed the same electron diffusion tendency related to mobility in the cubic phase. The m_h^*/m_0 values of the MAPb(Ni)I₃ and MAPb(Co)I₃ perovskite crystals were estimated to be 0.05 and 0.72, respectively, which were comparable with that of the MAPbI₃ perovskite crystal (0.02). Carrier diffusion related to hole mobility was inversely proportional with m^* for the MAPb(Ni)I₃ perovskite crystal and was higher than that of the MAPb(Co)I₃ perovskite crystal. This indicated that

the MAPb(Ni)I₃ perovskite crystal could promote photoinduced carrier diffusion, which led to an increase in charge carrier mobility and J_{sc} and a decrease in R_s . The calculated and experimental E_g values for the MAPbI₃, MAPb(Co)I₃, and MAPb(Ni)I₃ perovskite crystals are listed in Table IV. The experimental E_g values were confirmed by the alignment of the band edges in EQE. The theoretical and experimental E_g values of the perovskite crystals were similar. The ab initio quantum calculation EQE results using the GGA-PBE exchange-correlation function were lower than the experimental EQE values. These results indicated that E_g was affected by the crystal structure and phase.^{23,25}

The PDOS including occupancies, energy levels of the 2*p* and 3*d* orbitals of I, N, Pb, Co, and Ni near the VB and CB of the MAPbI₃, MAPb(Ni)I₃, and MAPb(Co)I₃ perovskite crystals were analyzed, and the results are presented in Fig. 10a, b, and c. The 2*p* orbitals of the I atom and 2*p* orbitals of the Pb atoms were located near the VB and CB levels of the reference MAPbI₃ perovskite crystal. For the MAPb(Ni)I₃ perovskite crystal, the 3*d* orbitals of the Ni atoms were partially hybridized with the 2*p* orbitals of the I atoms near the VB levels. The ligand-to-metal charge transfer promoted photoinduced carrier generation. The holes easily diffused

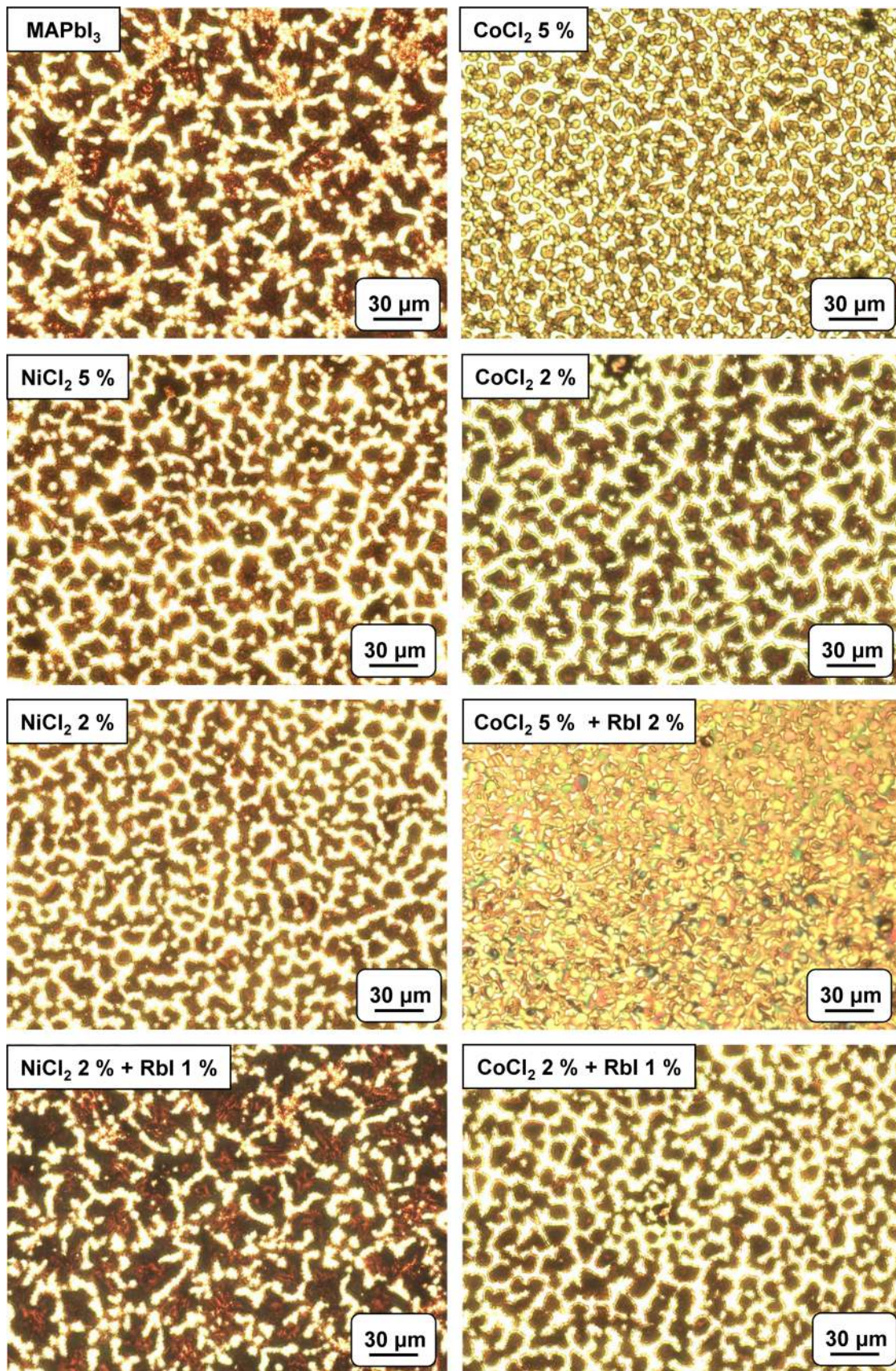


Fig. 6. Optical microscope images of the perovskite crystals with CoCl₂, NiCl₂, and RbI.

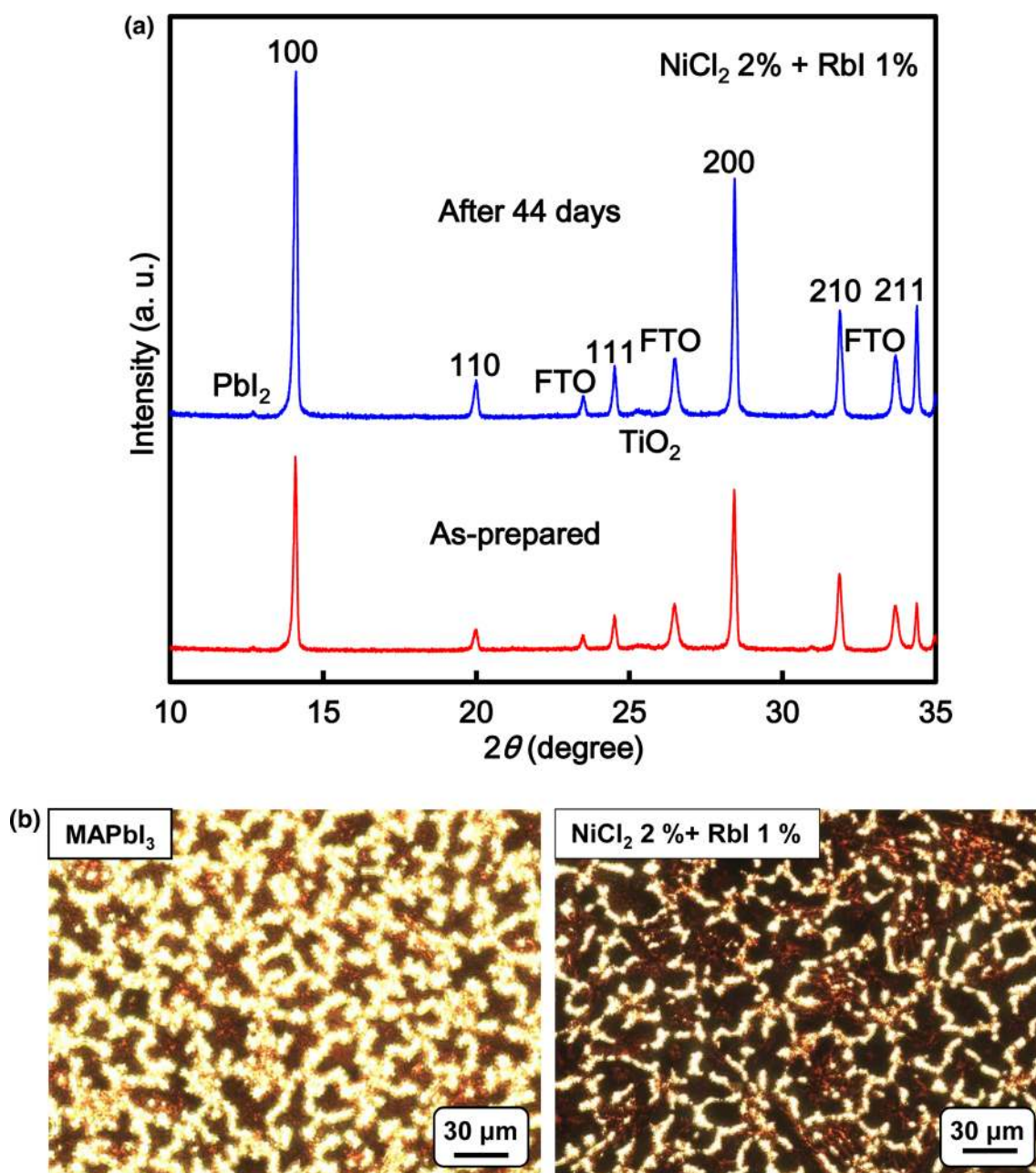


Fig. 7. (a) X-ray diffraction patterns of the MAPbI_3 perovskite solar cells with NiCl_2 and RbI after 44 days and (b) optical microscope images after 60 days. The samples were stored and characterized at temperature of 27°C and humidity of 20%.

around the VB, which suggested that hole mobility, which was related to J_{sc} and η , improved. For the $\text{MAPb}(\text{Co})\text{I}_3$ perovskite crystals, the $3d$ orbitals of Co with strong PDOS were localized above the VB. The $2p$ orbitals of the I atoms were slightly shifted near the VB and presented a wide energy dispersion, which caused an increase in the efficiency mass related to carrier mobility. The ligand-to-metal charge transfer was not caused by the localization of the $3d$ orbitals of Co atoms. For the $\text{MAPb}_{0.9}\text{Co}_{0.1}\text{I}_3$ crystal, the contribution of the $3d$ orbitals of the Co atoms near the VB promoted charge transfer, resulting in enhanced hole

mobility.²⁴ In this study, electrons and holes were not generated and did not diffuse near the CB and VB. The wide dispersion of the band structure was responsible for the decrease in η and J_{sc} with diffusion suppression in the perovskite crystal.

The calculated IR and Raman vibration modes of the $\text{MAPb}(\text{Ni})\text{I}_3$ and MAPbI_3 perovskite crystals are illustrated in Fig. 11a, b, c, and d. The IR and Raman vibration modes in the wide wavenumber range of $1000\text{--}4000\text{ cm}^{-1}$ were assigned to the bending modes of the N–C and N–H bonds of MA. The high intensity of the vibration modes in the IR and Raman spectra was ascribed to stretching of the

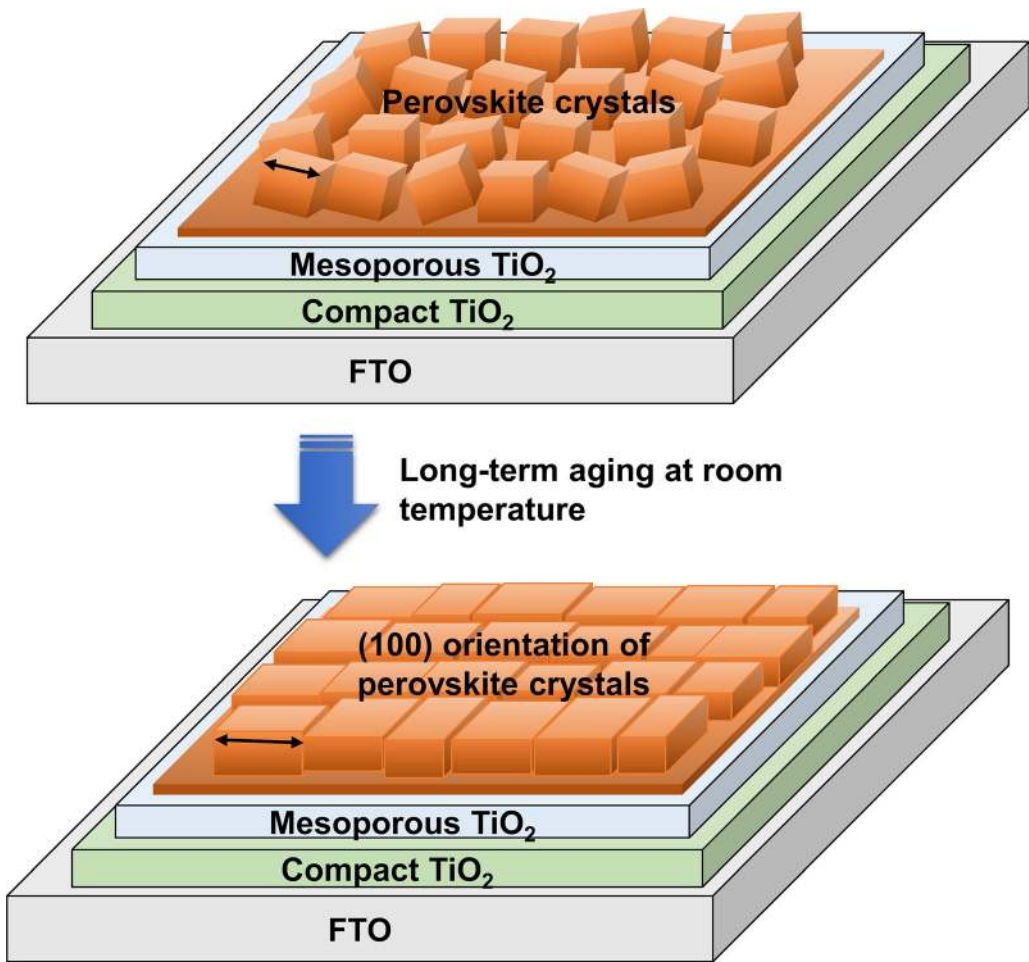


Fig. 8. Change in the surface morphology and crystal growth after long-term aging.

Table III. Changes in the particle sizes and surface coverages on the perovskite layer after 60 days

Devices	Particle size (μm)		Surface coverage (%)	
	As-prepared	After 60 days	As-prepared	After 60 days
MAPbI_3	13.0	3.4	61.5	48.2
NiCl_2 2% + RbI 1%	14.5	25.1	70.3	84.7

Pb–I bonds in the narrow wavenumber range of 20–200 cm^{-1} . The calculated IR and Raman vibration modes of the MAPbI_3 perovskite crystal were similar to the experimental data.^{28,34–36} The IR and Raman vibration modes of the $\text{MAPb}(\text{Ni})\text{I}_3$ crystal were attributed to the asymmetric stretching of the Ni–I bonds in the coordination structure.²⁵ The stretching modes of $\text{MAPb}(\text{Ni})\text{I}_3$ were downshifted compared with those of the reference MAPbI_3

perovskite crystal. The strength of the IR vibration modes was slightly lower and wider at the low wavenumber of 150 cm^{-1} . The IR vibration modes were attributed to the change in dipole moment associated with changes in vibration and bending. The Raman vibration modes were remarkably higher and wider at the wavenumbers of 60, 100, and 150 cm^{-1} . The Raman stretching vibration mode of the Pb–I bonds was associated with changes

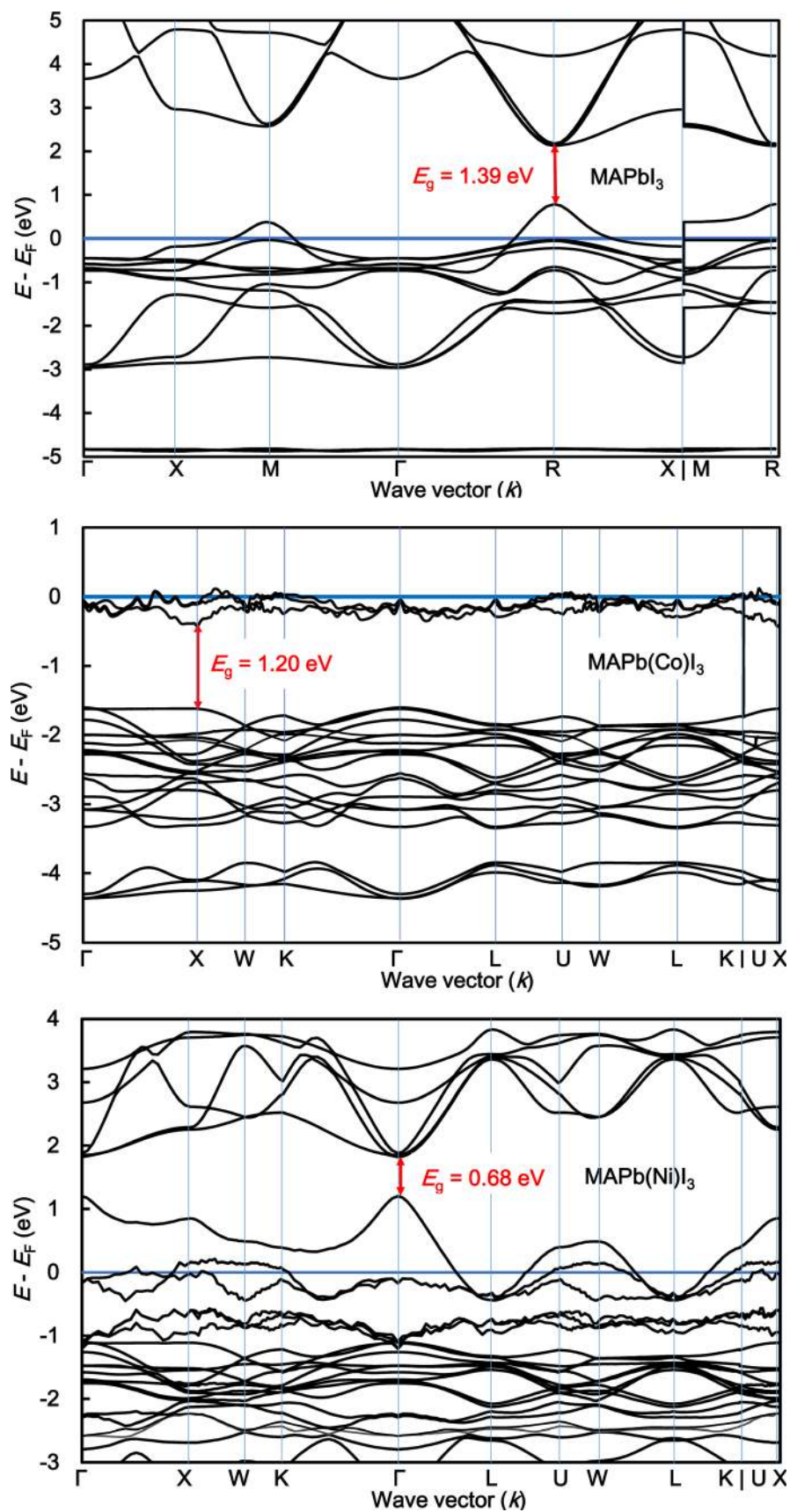


Fig. 9. Calculated band structures of the perovskite crystals.

Table IV. Effective mass ratios of electrons and holes, m_e^*/m_0 and m_h^*/m_0 , related to the electron mass m_0 and band gap energies of the perovskite crystals

Devices	Effective mass ratio (m^*/m_0)		Band gap (E_g)		
	m_e^*/m_0	m_h^*/m_0	Cal. (eV)	Exp. (eV)	Ref. (eV)
MAPbI ₃	0.01	0.02	1.394	1.563	1.56*
MAPb(Co)I ₃	0.04	0.72	1.198	1.547	1.56*
MAPb(Ni)I ₃	0.05	0.05	0.697	1.545	1.64**

*Ref. 23

** Ref. 25

in the polarization and distortion of the coordination structure near the ligand field. The vibration mode was similar to those of Cu- or Cr-incorporated FAPbI₃ perovskite crystals.²⁸ This vibrational behavior was related to the thermodynamic behavior based on electron–lattice interaction as a phonon effect. The electron–lattice interactions affected carrier diffusion related to carrier mobility. Details on the phonon effect in perovskite crystal can be found from the phonon dispersion. The decomposition was analyzed based on the experimental IR and Raman stretching vibration modes of the Pb–I and N–H bonds.

The thermodynamic parameters of the metal-incorporated MAPbI₃ perovskite cubic crystals with $2 \times 2 \times 2$ supercells used as cluster models were estimated using thermodynamic calculations. The ΔG , ΔH , and ΔS values of the MAPbI₃, MAPb(Ni)I₃, and MA(Rb)Pb(Ni)I₃ crystals are listed in Table V. The ΔG values of the MAPb(Ni)I₃ and MA(Rb)Pb(Ni)I₃ crystals were lower than that of the reference MAPbI₃ crystal. The thermodynamic stability of the perovskite crystals was improved by the addition of Ni and Rb to MAPbI₃. The theoretical results of the cluster models were qualitatively considered, as compared with the reported data.^{48–50} The thermodynamic stability of the perovskite crystals depended on the lattice unit volume per the number of formula units in the unit cell of the perovskite crystal. The lattice energy, ΔG , ΔH , and ΔS values were determined as the differences between the corresponding values of the reactants and products for each reaction. For the metal-added perovskites, the reaction processes and paths under actual conditions were not confirmed using the thermal properties and transient measurements using experimental data. It is difficult to quantitatively compare the theoretical and experimental results. The contribution of ΔG was dominated by an

increase in ΔS . For the Ni-incorporated MAPbI₃ perovskite crystals, ΔS depended on the electron–lattice interactions as a phonon effect related to the stretching mode of the Ni–I bonds in the low wavenumber range. The electron–lattice interactions suppressed carrier diffusion related to the decrease in carrier mobility and, consequently, J_{sc} and η decreased. The photovoltaic and optical properties of the MAPb(Ni)I₃ and MA(Rb)Pb(Ni)I₃ perovskite crystals were associated with the electronic correlation while suppressing the electron–lattice interaction as the phonon effect in the perovskite uniform layer with high orientation and crystal growth. Therefore, the incorporation of Ni and Rb into the MAPbI₃ perovskite crystals improved the crystallinity of the perovskite layer and slightly perturbed the coordination structure to optimize the electronic correlation, electron–lattice interactions, thermodynamic behavior, and stability of the perovskite. Controlling the electronic correlation by promoting the growth of defect-free crystals is important for improving the long-term stability of photovoltaic cells.

The long-term photovoltaic performance of the solar cells featuring MA(Rb)Pb(Ni)I₃, MAPb(Ni)I₃, and MAPb(Co)I₃ perovskite crystals was investigated and was compared with the previously reported results for solar cells featuring MAPb(Ni)I₃ and MAPb(Co)I₃ perovskite crystals.^{23–26} The photovoltaic solar cell featuring MA(Rb)Pb(Ni)I₃ perovskite crystals could achieve long-term stability by suppressing decomposition. In particular, partially replacing Pb²⁺ ions with Ni²⁺ ions and MA⁺ ions with Rb⁺ ions improved long-term stability and carrier mobility based on the effective mass in the crystal structure. However, the initial performance of these cells should be improved to promote their practical applications for photovoltaic devices. The photovoltaic performance of solar cells was assessed

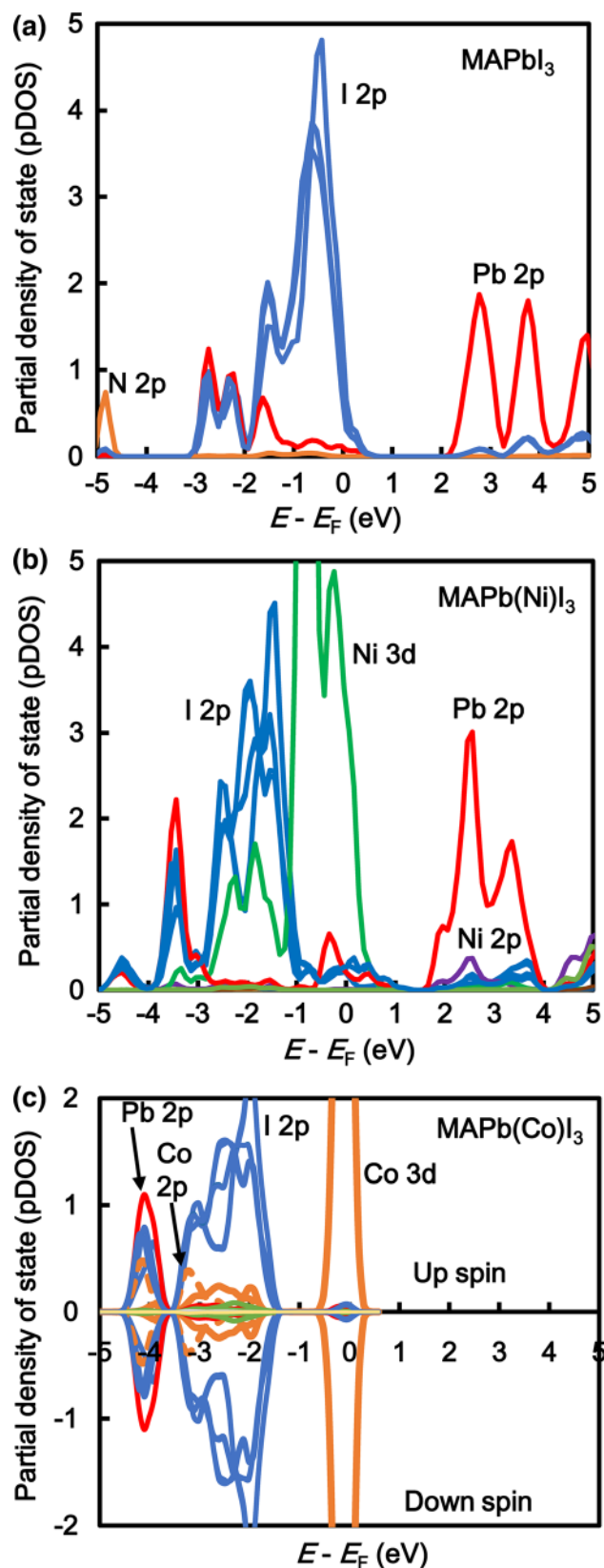


Fig. 10. Partial density of states of (a) MAPbI_3 , (b) MAPb(Ni)I_3 , and (c) MAPb(Co)I_3 perovskite crystals.

based on the surface modification and coverage, crystal growth, and high (100) orientation in the perovskite layer. Compared to the surface conditions and crystal structures of the previously reported solar cells featuring alkali metals,^{23–26} the crystal nucleation and growth of the MA(Rb)Pb(Ni)I_3 crystals should be promoted and the occurrence of defects and pinholes should be suppressed. The highly accurate optimization of the film formation conditions and crystal nucleation and growth can confer long-term stability to photovoltaic cells, which would increase their potential for practical applications.

CONCLUSIONS

Ni- and Co-incorporated MAPbI_3 perovskite solar cells were fabricated and characterized, and their photovoltaic properties, crystal growth, and orientation were improved. The partial replacement of Pb^{2+} ions in the perovskite crystals with Ni^{2+} or Co^{2+} ions affected the photoinduced carrier generation and diffusion, effective mass, and metal-to-ligand charge transfer via hybridization between the 2p orbitals of I and the 3d orbitals of Ni near the VB. Additionally, the co-addition of Ni and Rb to MAPbI_3 perovskite crystals improved the long-term stability of the photovoltaic cells owing to crystal growth promotion and surface modification of the perovskite layer. The photovoltaic performance of the solar cells strongly depended on the (100) plane orientation, crystal growth, and surface coverage of the perovskite layer. J_{sc} and η were increased by promoting photoinduced carrier diffusion related to carrier mobility in inverse proportion with m^*/m_0 in the band dispersion. The promotion of carrier mobility associated with m_h/m_0 was ascribed to the metal-to-ligand charge transfer, which occurred via the hybridization of the 3d orbitals of Ni with the 2p orbitals of I near the VB. The ΔG values indicated the thermodynamic stability of the perovskite crystals co-added with Ni and Rb. The changes in ΔS were attributed to the electron–lattice interaction owing to the phonon effect. Photovoltaic mechanisms were associated with the competition between the electron correlation based on the metal-to-ligand charge transfer, electron–lattice interaction as a phonon effect, and thermodynamic stability. The electronic correlation was derived from the charge transfer and exchange interactions between the localized 3d orbitals of Ni and the 2p orbitals of I^- ion ligands in the coordination structure. The co-addition of Ni and Rb to the perovskite crystals improved the long-term stability of photovoltaic cells. The long-term stability was attributed to the promotion of crystal growth and orientation and the surface modification of the perovskite layer.

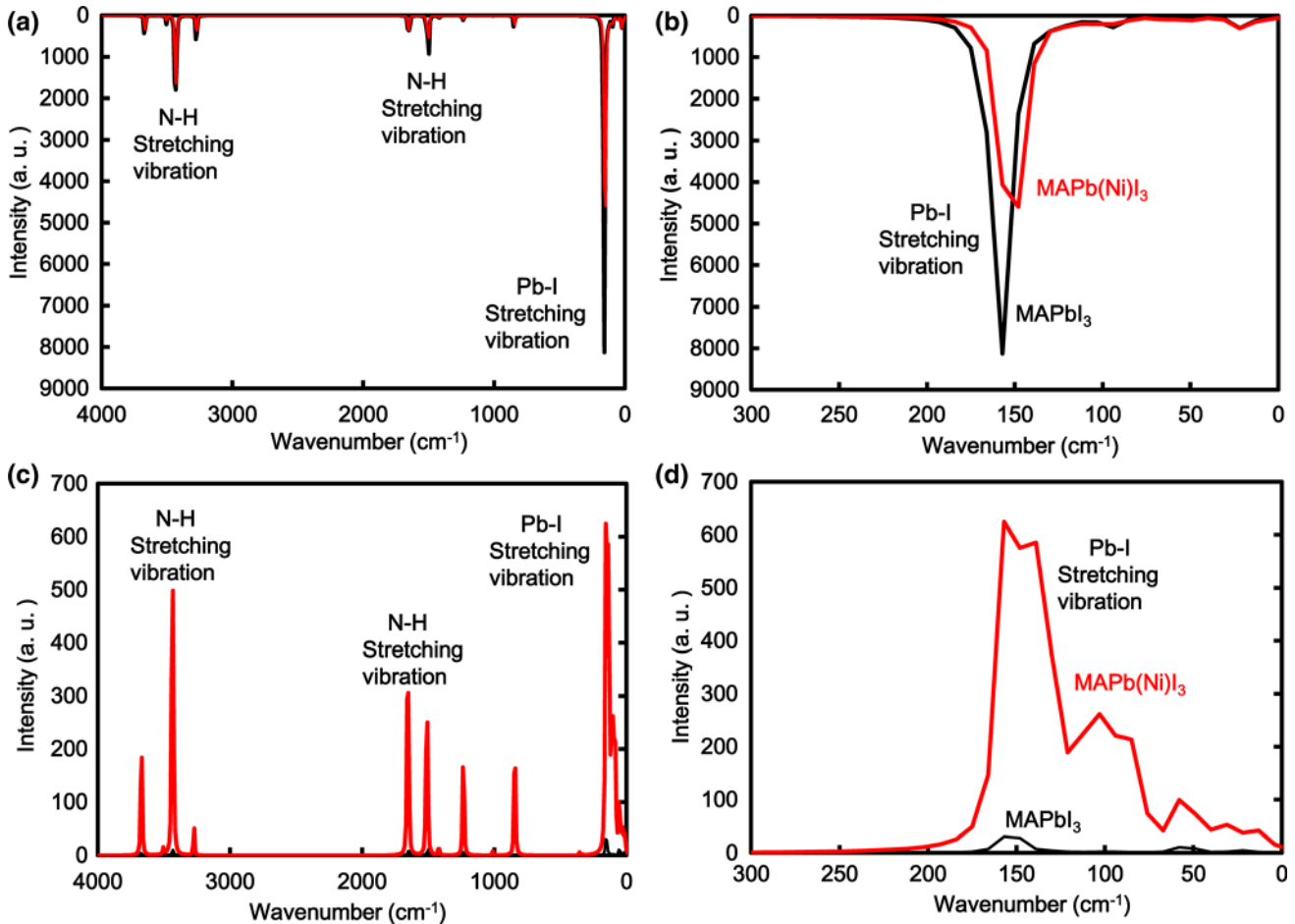


Fig. 11. Calculated vibration modes in (a), (b) IR and (c), (d) Raman spectra of the MAPb(Ni)I₃ and MAPbI₃ crystals in the normal (a) and (c), and (b), (d) enlarged view (a) and (c).

Table V. Enthalpy, entropy, and Gibbs free energies of MAPbI₃, MAPb(Ni)I₃, and MA(Rb)Pb(Ni)I₃ perovskite crystals

Device	MAPbI ₃	MAPb(Ni)I ₃	MA(Rb)Pb(Ni)I ₃
Enthalpy H (kJ mol ⁻¹)	2307	2308	2083
Entropy S (J K ⁻¹ mol ⁻¹)	4219	4318	4308
Gibbs free energy G (kJ mol ⁻¹)	1054	1025	803

CONFLICT OF INTEREST

The authors declare that they have no conflict of interest.

REFERENCES

1. N.J. Jeon, J.H. Noh, W.S. Yang, Y.C. Kim, S. Ryu, J. Seo, and S.I. Seok, *Nature*, 2015, **517**, p 476.
2. M. Saliba, T. Matsu, J.Y. Seo, K. Domanski, J.P.C. Baena, M.K. Nazeeruddin, S.M. Zakeeruddin, W. Tress, A. Abate, A. Hagfeldt, and M. Grätzel, *Energy Environ. Sci.*, 2016, **9**, p 1989.
3. S.P. Dunfield, L. Bliss, F. Zhang, J.M. Luther, K. Zhu, M.F.A.M. Hest, M.O. Reese, and J.J. Berry, *Adv. Energy Mater.*, 2020, **10**, p 1904054.
4. D.P. McMeekin, G. Sadoughi, W. Rehman, G.E. Eperon, M. Saliba, M.T. Hörantner, A. Haghighirad, N. Sakai, L. Korte, B. Rech, M.B. Johnston, L.M. Herz, and H.J. Snaith, *Science*, 2016, **351**, p 151.
5. A. Suzuki, H. Okada, and T. Oku, *Energies*, 2016, **9**, p 376.
6. Y. Umemoto, A. Suzuki, and T. Oku, *AIP Conf. Proc.*, 2017, **1807**, p 020011.
7. A.D. Jodlowski, C.R. Carmona, G. Grancini, M. Salado, M. Ralaierisoa, S. Ahmad, N. Koch, L. Camacho, G. Miguel, and M.K. Nazeeruddin, *Nat. Energy*, 2017, **2**, p 972.
8. M.I. Saidaminov, J. Kim, A. Jain, R.Q. Bermudez, H. Tan, G. Long, F. Tan, A. Johnston, Y. Zhao, O. Voznyy, and E.H. Sargent, *Nat. Energy*, 2018, **3**, p 648.
9. J. Tong, Z. Song, D.H. Kim, X. Chen, C. Chen, A.F. Palmstrom, P.F. Ndione, M.O. Reese, S.P. Dunfield, O.G. Reid, J. Liu, F. Zhang, S.P. Harvey, Z. Li, S.T. Christensen, G. Teeter, D. Zhao, M.M.A. Jassim, M.F.A.M. Hest, M.C. Beard, S.E. Shaheen, J.J. Berry, Y. Yan, and K. Zhu, *Science*, 2019, **364**, p 475.

10. S. Bai, P. Da, C. Li, Z. Wang, Z. Yuan, F. Fu, M. Kawecki, X. Liu, N. Sakai, J.T.W. Wang, S. Huettner, S. Buecheler, M. Fahlman, F. Gao, and H.J. Snaith, *Nature*, 2019, **571**, p 245.
11. A. Suzuki, M. Kato, N. Ueoka, and T. Oku, *J. Electron. Mater.*, 2019, **48**, p 3900.
12. Y. Wang, M.I. Dar, L.K. Ono, T. Zhang, M. Kan, Y. Li, L. Zhang, X. Wang, Y. Yang, X. Gao, Y. Qi, M. Grätzel, and Y. Zhao, *Science*, 2019, **365**, p 591.
13. W. Zhao, Z. Yao, F. Yu, D. Yang, and S. Liu, *Adv. Sci.*, 2017, **5**, p 1700131.
14. Z. Tanga, S. Uchida, T. Bessho, T. Kinoshita, H. Wang, F. Awai, R. Jono, M.M. Maitani, J. Nakazaki, T. Kubo, and H. Segawa, *Nano Energy*, 2018, **45**, p 184.
15. Y. Chen, N. Li, L. Wang, L. Li, Z. Xu, H. Jiao, P. Liu, C. Zhu, H. Zai, M. Sun, W. Zou, S. Zhang, G. Xing, X. Liu, J. Wang, D. Li, B. Huang, Q. Chen, and H. Zhou, *Nat. Commun.*, 2019, **10**, p 1112.
16. T. Oku, S. Kandori, M. Taguchi, A. Suzuki, M. Okita, S. Minami, S. Fukunishi, and T. Tachikawa, *Energies*, 2020, **13**, p 4776.
17. T. Nakamura, S. Yakumaru, M.A. Truong, K. Kim, J. Liu, S. Hu, K. Otsuka, R. Hashimoto, R. Murdey, T. Sasamori, H.D. Kim, H. Ohkita, T. Handa, Y. Kanemitsu, and A. Wakamiya, *Nat. Commun.*, 2020, **11**, p 3008.
18. D. Cortecchia, H.A. Dewi, J. Yin, A. Bruno, S. Chen, T. Baikie, P.P. Boix, M. Grätzel, S. Mhaisalkar, C. Soci, and N. Mathews, *Inorg. Chem.*, 2016, **55**, p 1044.
19. N. Ueoka, and T. Oku, *ACS Appl. Energy Mater.*, 2020, **3**, p 7272.
20. N. Ueoka, T. Oku, and A. Suzuki, *RSC Adv.*, 2019, **9**, p 24231.
21. S. Ye, H. Rao, Z. Zhao, L. Zhang, H. Bao, W. Sun, Y. Li, F. Gu, J. Wang, Z. Liu, Z. Bian, and C. Huang, *J. Am. Chem. Soc.*, 2017, **139**, p 7504.
22. K.L. Wang, R. Wang, Z.K. Wang, M. Li, Y. Zhang, H. Ma, L.S. Liao, and Y. Yang, *Nano Lett.*, 2019, **19**, p 5176.
23. M.T. Klug, A. Osherov, A.A. Haghighirad, S.D. Stranks, P.R. Brown, S. Bai, J.T.W. Wang, X. Dang, V. Bulovi, H.J. Snaith, and A.M. Belcher, *Energy Environ. Sci.*, 2017, **10**, p 236.
24. W. Xu, L. Zheng, X. Zhang, Y. Cao, T. Meng, D. Wu, L. Liu, W. Hu, and X. Gong, *Adv. Energy Mater.*, 2018, **8**, p 1703178.
25. X. Gong, L. Guan, H. Pan, Q. Sun, X. Zhao, H. Li, H. Pan, Y. Shen, Y. Shao, L. Sun, Z. Cui, L. Ding, and M. Wang, *Adv. Funct. Mater.*, 2018, **28**, p 1804286.
26. H. Zheng, G. Liu, X. Xu, A. Alsaedi, T. Hayat, X. Pan, and S. Dai, *Chemsuschem*, 2018, **11**, p 3269.
27. A. Kooijman, L.A. Muscarella, and R.M. Williams, *Appl. Sci.*, 2019, **9**, p 1678.
28. A. Suzuki, and T. Oku, *Heliyon*, 2018, **4**, p e00755.
29. H.X. Zhu, X.H. Wang, and G.C. Zhuang, *Appl. Phys. A*, 2019, **125**, p 45.
30. T. Oku, *Rev. Adv. Mater. Sci.*, 2020, **59**, p 264.
31. M. Pazoki, and T. Edvinsson, *Sustain. Energy Fuels*, 2018, **2**, p 1430.
32. L. Wang, H. Zhou, J. Hu, B. Huang, M. Sun, B. Dong, G. Zheng, Y. Huang, Y. Chen, L. Li, Z. Xu, N. Li, Z. Liu, Q. Chen, L.D. Sun, and C.H. Yan, *Science*, 2019, **363**, p 265.
33. S. Yang, H. Zhao, Y. Han, C. Duan, Z. Liu, and S.F. Liu, *Small*, 2019, **15**, p 1904387.
34. M.A.P. Osorio, Q. Lin, R.T. Phillips, R.L. Milot, L.M. Herz, M.B. Johnston, and F. Giustino, *J. Phys. Chem. C*, 2018, **122**, p 21703.
35. K. Nakada, Y. Matsumoto, Y. Shimoi, K. Yamada, and Y. Furukawa, *Molecules*, 2019, **24**, p 626.
36. J.I. Jaña, R. Mueyudinov, P. Rosado, H. Mirhosseini, M. Chugh, O. Nazarenko, D.N. Dirin, D. Heinrich, M.R. Wagner, T.D. Kühne, B. Szyszka, M.V. Kovalenko, and A. Hoffmann, *Phys. Chem. Chem. Phys.*, 2020, **22**, p 5604.
37. D.J. Kubicki, D. Prochowicz, A. Hofstetter, S.M. Zakeeruddin, M. Grätzel, and L. Emsley, *J. Am. Chem. Soc.*, 2017, **139**, p 14173.
38. D.J. Kubicki, D. Prochowicz, A. Hofstetter, S.M. Zakeeruddin, M. Grätzel, and L. Emsley, *J. Am. Chem. Soc.*, 2018, **140**, p 7232.
39. E.A. Alharbi, A.Y. Alyamani, D.J. Kubicki, A.R. Uhl, B.J. Walder, A.Q. Alanazi, J. Luo, A.B. Caminal, A. Albadri, H. Albrithen, M.H. Alotaibi, J.E. Moser, S.M. Zakeeruddin, F. Giordano, L. Emsley, and M. Grätzel, *Nat. Commun.*, 2019, **10**, p 3008.
40. J.V. Milić, J.H. Im, D.J. Kubicki, A. Ummadisingu, J.Y. Seo, Y. Li, M.A.R. Preciado, M.I. Dar, S.M. Zakeeruddin, L. Emsley, and M. Grätzel, *Adv. Energy Mater.*, 2019, **9**, p 1900284.
41. L. Qiu, S. He, L.K. Ono, and Y. Qi, *Adv. Energy Mater.*, 2020, **10**, p 1902726.
42. C. Wang, B.R. Ecker, H. Wei, J. Huang, J.Q. Meng, and Y. Gao, *Phys. Chem. Chem. Phys.*, 2017, **19**, p 5361.
43. A. Suzuki, and T. Oku, *Appl. Surf. Sci.*, 2019, **483**, p 912.
44. A. Suzuki, Y. Miyamoto, and T. Oku, *J. Mater. Sci.*, 2020, **55**, p 9728.
45. C. Paschal, A. Pogrebnoi, T. Pogrebnaya, and N. Seriani, *SN Appl. Sci.*, 2020, **2**, p 718.
46. C. Zhang, and X. Luo, *RSC Adv.*, 2020, **10**, p 23743.
47. T. Liu, Y. Li, S. Feng, W. Yang, R. Xu, X. Zhang, H. Yang, and W. Fu, *ACS Appl. Mater. Interfaces*, 2020, **12**, p 904.
48. A. Cicciole, and A. Latini, *Phys. Chem. Lett.*, 2019, **9**, p 3756.
49. A. Senocrate, G.Y. Kim, M. Grätzel, and J. Maier, *ACS Energy Lett.*, 2019, **4**, p 2859.
50. S.K.A. Aal, and A.S.A. Rahman, *J. Cryst. Growth*, 2017, **457**, p 282.